Fatigue Crack Path in 2xxx Aluminum Alloys at 223K

C. GASQUERES [1,2], C. SARRAZIN-BAUDOUX [1] and J. PETIT [1]

[1] LMPM/ENSMA, UMR CNRS 6617, Chasseneuil-Futuroscope, France
[2] Centre de Recherches Alcan, Voreppe, France

ABSTRACT. *The Fatigue Crack Growth behavior of new generation 2xxx aluminum alloys has been investigated at 223K in comparison to room temperature. Crack growth rates are not influenced by a cold and dry environment in the peak aged temper but are one order of magnitude slower in the naturally aged temper. Such retarded crack propagation is associated to a highly crystallographic crack path. Results are discussed on the basis of a model for intrinsic and environmentally assisted crack propagation.*

INTRODUCTION

Aluminum alloys used for aircraft structures are commonly confronted with high altitude rarefied atmosphere at a temperature of about 223K. While number of studies [1-6] aim to fatigue properties as influenced by environmental conditions, very few [7, 8] are devoted to damage tolerance at low temperature. This paper deals with a comparative study of the fatigue crack propagation resistance of two new generation aluminum alloys tested at low temperature (223K) in dry air (dew point of 223K) (environment labeled as "cold air") in comparison to ambient air (about 50%RH) at room temperature and to high vacuum considered as a reference inert environment.

Results are analyzed on the basis of scanning observations of the cracked surfaces and of the modeling framework initially proposed for Al alloys by Petit [3] and thus extended to most of the metallic alloys by Petit et al. [6] for intrinsic crack propagation and environmentally assisted crack propagation.

.

EXPERIMENTAL

The alloys used in the present study were provided by Alcan in form of 40 mm thick plates of Al-Cu-Mg 2024A alloy in the T351 temper, and of Al-Cu-Mg 2022 alloy in the T351 and T851 tempers. As is illustrated in Figure 1 for the 2024A alloy, the microstructures of both alloys are very similar and consist of grains elongated in the rolling direction (670x200x80 μm3). In naturally aged temper, the hardening precipitation consists in coherent Al-Cu Guinier-Preston (GP) zones mixed with Al-Cu-Mg GP(B) zones which are predominant in the 2024A alloy and few in the 2022 alloy. The peak-aged heat treatment of the 2022 alloy is the standard temper designation T851

and consists of predominant semi-coherent θ' needles (Al_2Cu) of about 100 nm length and a few S' (Al_2CuMg) precipitates.

The main mechanical properties at room temperature and 223K are listed in Table 1.

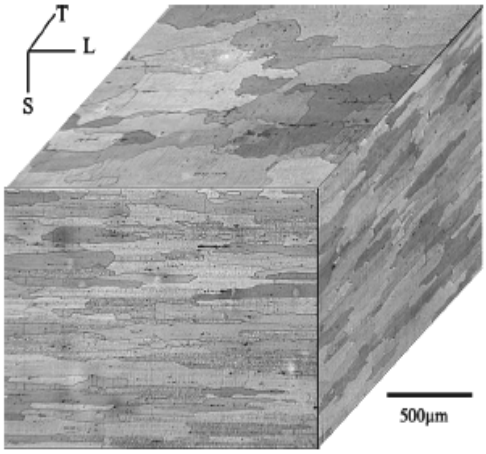

Figure 1: microstructure of 2024A as obtained after Keller etches.

Table 1: Mechanical properties of the studied alloys at 300K and 223 K

		300 K			223 K		
		R0.2 (MPa)	Rm (MPa)	A%	R0.2 (MPa)	Rm (MPa)	A%
2022	T351	291	395	27.1	304	406	27.1
	T851	381	443	14.0	394	456	14.5
2024A	T351	356	467	21.2	364	474	24.0

Fatigue crack growth tests were performed on a servo hydraulic testing machine under load control. The loading signal was a sinusoidal waveform with a frequency of 35 Hz and a load ratio (R) of 0.1. The compact tension specimens were machined for a crack plane having an LT orientation with a width W of 50 mm and a thickness B of 10 mm. The crack length, a, was recorded with a traveling microscope. Following precracking in air at a constant ΔK range of 12 MPa√m, threshold tests were performed using a load shedding procedure following the ASTM recommendation (E 647). After the attainment of the threshold range ΔK_{th}, a constant load test was performed up to the near-failure domain. Crack closure measurements were carried out using the compliance method, by means of a capacitive gauge mounted at the mouth of the notch of the specimens. The

temperature control of the specimen was achieved via four blocks of aluminum alloy fixed on the back of the specimens [7]. These blocks were cooled by means of silicon oil circulating from an external cooling source. The dew point in the atmosphere was controlled with a high precision hygrometer, the dry air being provided by an external apparatus. High vacuum tests were conducted at 223K and 300K inside the environmental chamber allowing a low pressure of $3x10^{-4}$ Pa.

INFLUENCE OF COLD TEMPERATURE

The Fatigue Crack Growth rates (da/dN) in ambient air (300K) and in cold air (223K) are plotted in Figure 2 with respect to the ΔK range. The curves obtained at 300K for the three alloys are quite similar with a slightly better resistance against crack propagation for the 2022 T351 in the lower rate range. The threshold ranges are about 5 MPa√m, 4.5 MPa√m and 4 MPa√m for the 2022T851, 2024AT351 and 2022T351 alloys respectively.

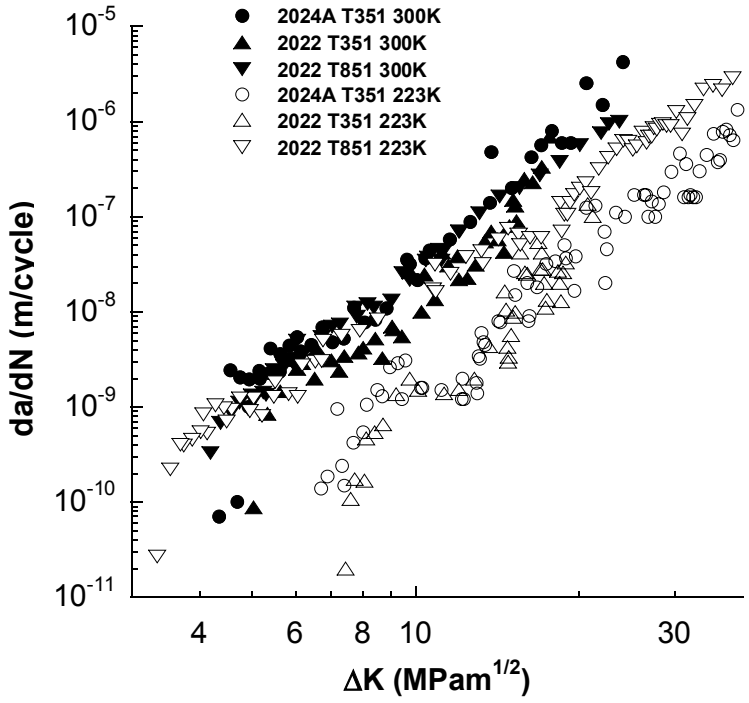

Figure 2: Influence of temperature on the crack propagation rate: ambient air (300K) and cold air (223) at R=0.1 and 35Hz.

At 223K, a marked effect of temperature for the two alloys for the T351 temper consists in a substantial reduction of the crack growth rates and a large increase in the

threshold ranges, i.e. about 6.5 MPa√m and 7.3 MPa√m for the 2024AT351 and 2022T351 alloys respectively, compared to 3.4 MPa√m for the 2022T851. Observations of the fracture surfaces by mean of a scanning microscope as illustrated in Figure 3a, show that the retarded crack propagation in the naturally aged alloys is associated to a crystallographic crack path in contrast with the flat crack path observed at 223K on the 2022 in the peak aged temper T851 (Figure 3b), which is comparable to that obtained at room temperature with a slightly slower propagation in at mid ΔK (Paris regime), but with a lower threshold ranging about 3.4 MPa√m.

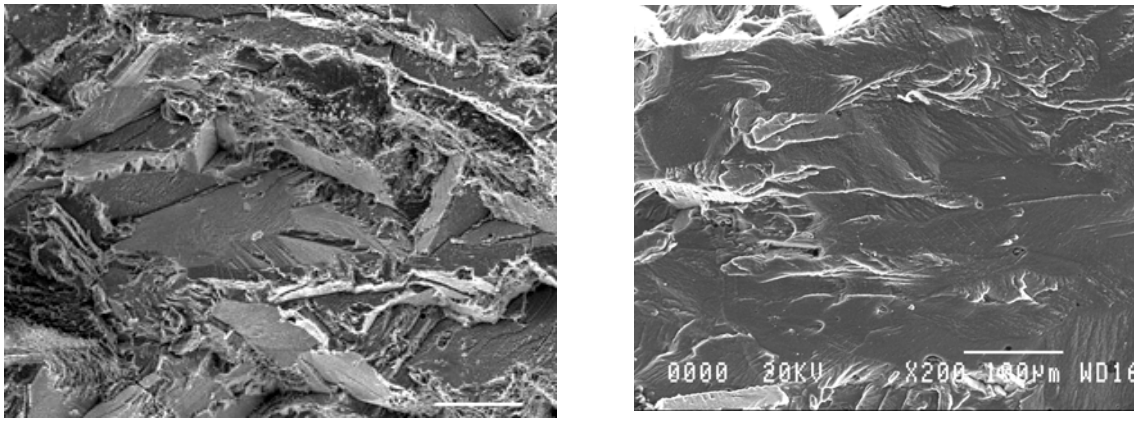

a) b)

Figure 3: a) 2024A T351: crystallographic crack path in dry air at 223K;
b) 2022 T851: stage II crack path in air at 300K.

INFLUENCE OF ENVIRONMENT

Figures 4a and 4b compare the crack propagation curves obtained in air and high vacuum for the three alloys at 300K and 223K respectively. At room temperature (Figure 4a), the curves for the 2022T851 in both environments are very similar and, consequently, there is no significant influence of air environment. But for the underaged alloys the crack growth rates in high vacuum are substantially slower than in air (more than one order of magnitude) and the threshold ranges are much higher (about 50%). This effect of environment consists in a change in the crack growth mechanism from a stage II regime to a crystallographic regime associated to a very rough crack path as observed previously in the literature on 7xxx and 2xxx alloys (3, 8, 9 and 10). At 223K, the influence of environment is low, while the influence of microstructure is high.

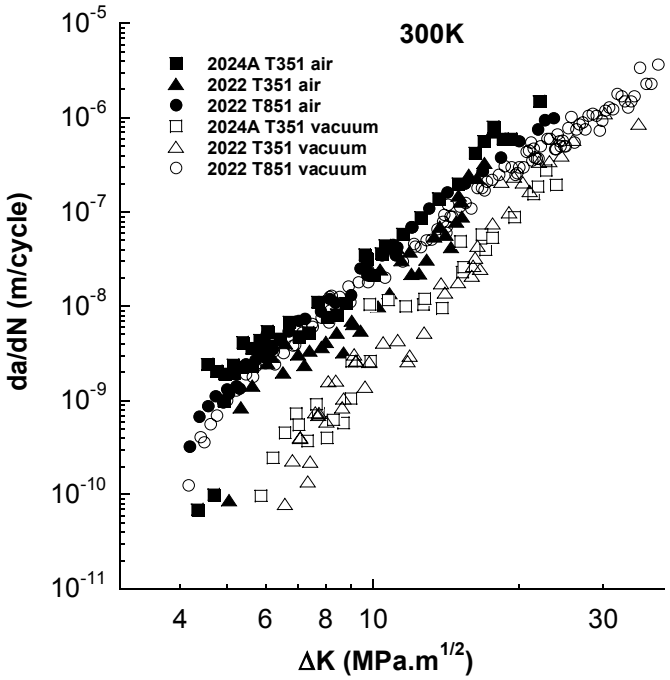

a)

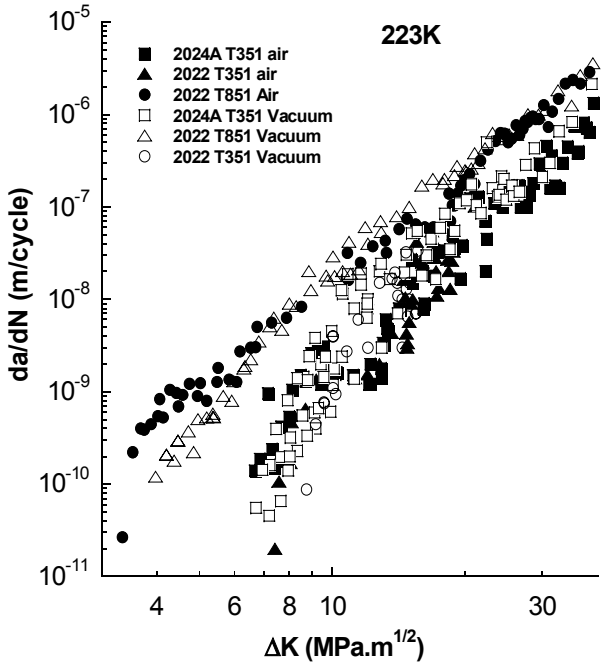

b)

Figure 4: Crack propagation curves da/dN vs ΔK in ambient air and high vacuum at room temperature (a) and 223K (b).

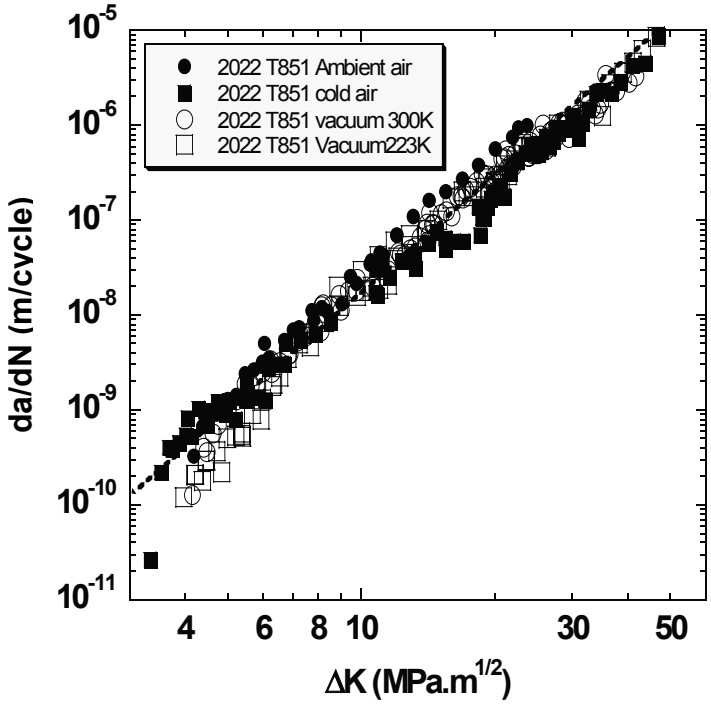

Figure 5: Crack propagation rates in air and high vacuum at 300K and 223K for the 2022 peakaged alloy

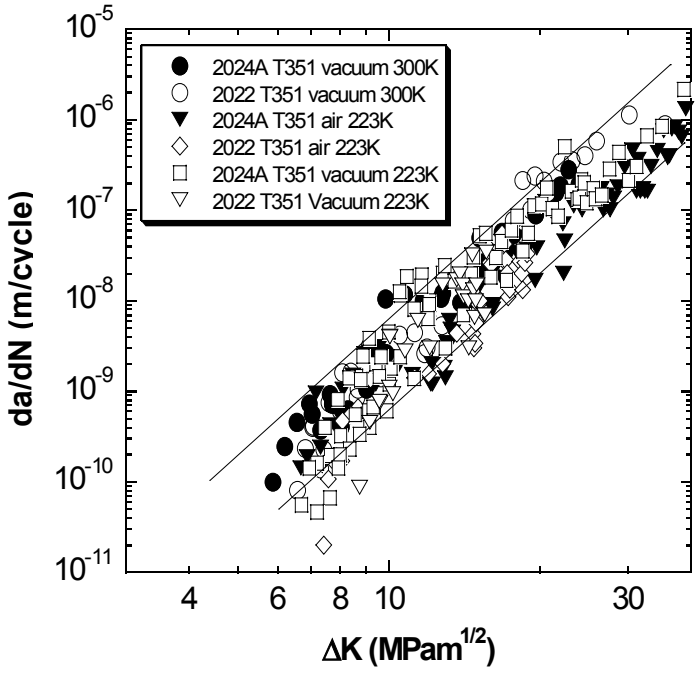

Figure 6: Crystallographic crack propagation in naturally aged 2024A and 2022 alloys in cold dry air and in high vacuum.

As is illustrated in Figure 5, the behavior of the 2022 T851 at 223K is similar to that at room temperature without detectable influence of environment except at growth rates lower than 10^{-9} m/cycle for which a slightly faster crack growth is detected in air.

For both naturally aged alloys (Figure 6) the behavior in dry air and in high vacuum is comparable and corresponds to the crystallographic regime observed in high vacuum at room temperature. Now the question arises to know whether the controlling factor is the air dryness or the temperature. At first sight, the results in high vacuum support primarily the hypothesis of an effect of air dryness. But in view of getting a clearer picture of the behavior of the alloys in the underaged temper at 223K, a more detailed examination of the crack propagation behavior has been carried out based on crack closure measurements so as to uncouple closure and environment effects.

INFLUENCE OF CRACK CLOSURE AND DISCUSSION

Crack closure, and particularly the roughness induced crack closure, is known to substantially influence the crack growth rates in the threshold domain [11]. In order to evaluate and eliminate the closure contribution, the effective stress intensity factor range ΔK_{eff} is measured in term of compliance variation as initially proposed by Elber [11]. In addition, to account for the change in the Young modulus (E) with temperature, the growth rates are plotted against ΔK_{eff} / E [13].

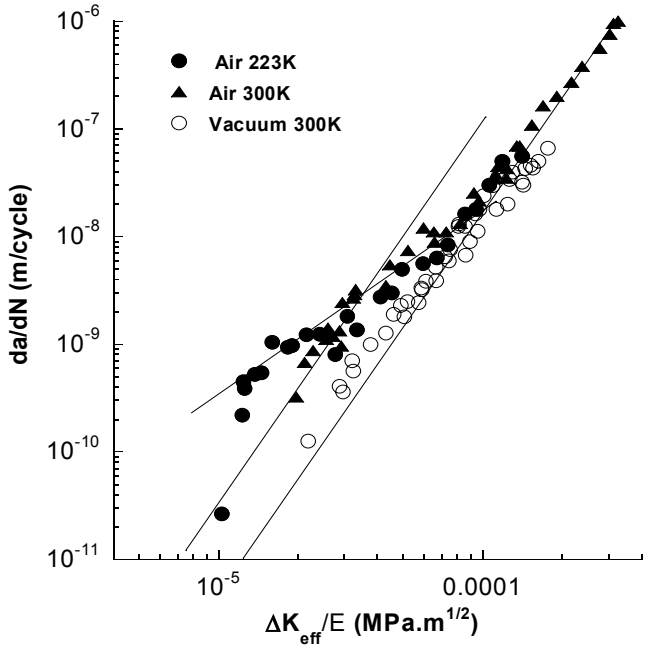

Figure 7: Effective fatigue crack propagation da/dN vs ΔK_{eff} / E for 2022 T851.

In Figure 7, the effective propagation curves da/dN vs $\Delta K_{eff}/E$ are plotted for the 2022 T851 alloy in air at both temperatures, and in high vacuum at room temperature. For da/dN higher than $5x10^{-9}$ m/cycle, there is no distinguishable influence of temperature and only a small effect of environment. But at lower growth rates, the influence of environment is more detected and more marked than on nominal curves (Figure 2).

These results are compared with the modeling framework initially proposed by J. Petit [13] and further detailed by [6, 10, 12, and 13].

For long cracks in polycrystalline Al alloys as well as for most of the metallic alloys, four propagation regimes have been highlighted (Figure 8):

i) Two intrinsic regimes operative in inert environment (high vacuum):

- The intrinsic stage II which is favored by peakaged and overaged microstructures containing large and semi-coherente or non-coherent precipitates, and by large plastic zone favoring the activation of different slip systems leading to homogeneous deformation and smooth crack path. An intrinsic propagation law has been derived [12, 13] as:

$$da/dN = A/D^*[\Delta Keff/E]^4 \quad (1)$$

where A is a dimensionless parameter and D* the critical cumulated displacement leading to rupture.

- The intrinsic stage I-like propagation which is favored by microstructures containing fine shearable precipitates such as GP zones in underaged Al alloys. The associated deformation is heterogeneously localized within each individual grain along the crack front. This leads to highly crystallographic crack propagation associated to tortuous crack path and enhanced roughness of fracture surfaces [3, 6, 8, 9, and 13]. This stage in polycristal is generally characterized by a strong retardation due to the barrier effect of grain boundaries [14]. The same relation as that for the intrinsic stage II (relation (1)) with a shielded value of the stress intensity factor range $\chi\ \Delta Keff$ as initially suggested by Suresh [15], with $0< \chi<1$, and χ depending on several factors as grain size, aged microstructure or anisotropy.

ii) Two environmentally assisted regimes operative in air and in moist atmospheres:

- Water vapor adsorption [6, 13, 16, 17] assisted stage II which has been described with a relation derived [6, 13] from that of the intrinsic stage II (relation (1)) with D* decreased by the adsorption process.

- Hydrogen assisted stage II propagation [6, 18] described by a relation derived from the initial models of McClintock [19] as

$$da/dN = B[\Delta K_{eff}^2/E\sigma] \quad (2)$$

where B is a dimensionless coefficient and σ a strength parameter.

The straight lines corresponding to the different regimes are plotted in Figure 8 to analyze the experimental data. They are directly extracted from the above presented modeling framework without any adjustable parameters. For the 2022 T851 alloy (Figure 8), the crack propagation behavior at growth rates higher than $5x10^{-9}$ m/cycle is consistent with the intrinsic stage II regime as confirmed by the fracture surface morphology illustrated in the Figure 9a. This regime is the same for the crack propagation in the three alloys in ambient air. For the 2022 T851, the stage II regime

prevails in vacuum at any crack growth rate down to the threshold, while in air, at rates lower than 5x10-9 m/cycle, an environment assistance explainable in term of water vapor adsorption is observed in the very near threshold domain; however, the available data are not sufficient to get a precise description of the process.

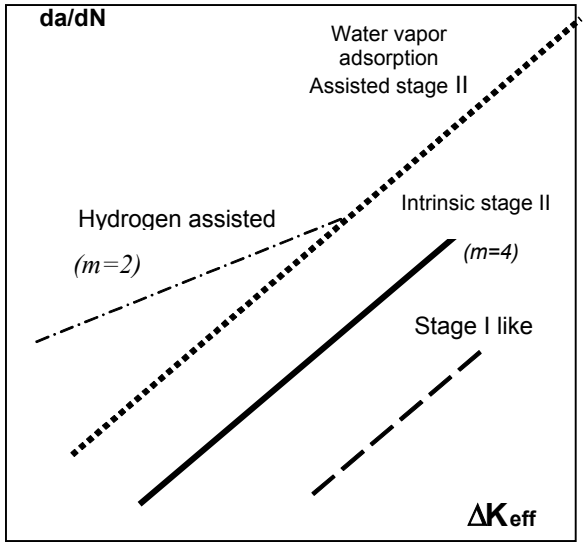

Figure 8: schematic illustration of crack propagation regimes [1, 15, and 16].

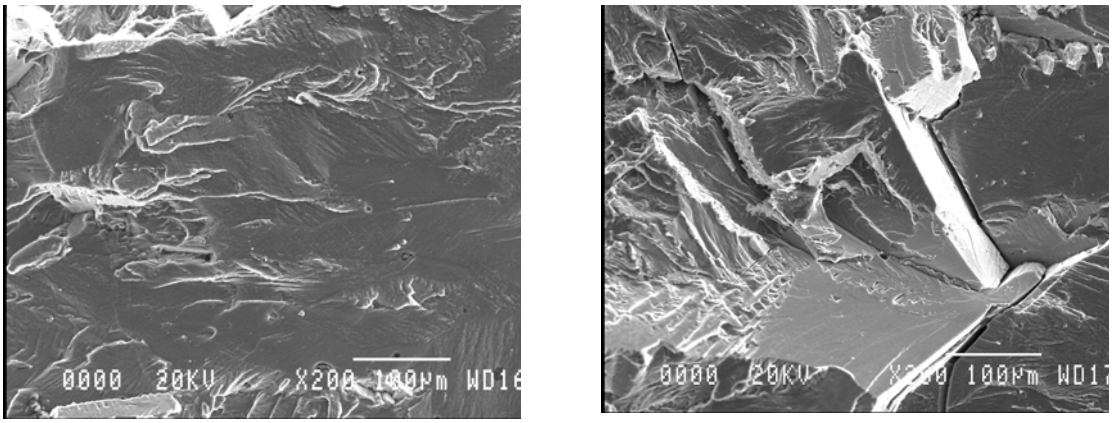

Figure 9: SEM fracture surface morphology at 223K.
a) 2022 T851: stage II regime in air; b) 2024A T351: stage I like regime in vacuum.

For the two naturally under aged alloys, the propagation curves are plotted in Figure 10 for the different test conditions. For both alloys, the crack behavior in ambient air is mainly in

accordance with water vapor assisted stage II propagation associated to a fracture surface morphology comparable to that of the 2022 T851 as is illustrated in figure 9a. For both alloys a substantial difference in the growth rates between ambient air and cold air curves is still present and obviously the crack closure phenomena cannot solely account for their much higher crack growth resistance at 223 K whatever the surface roughness.

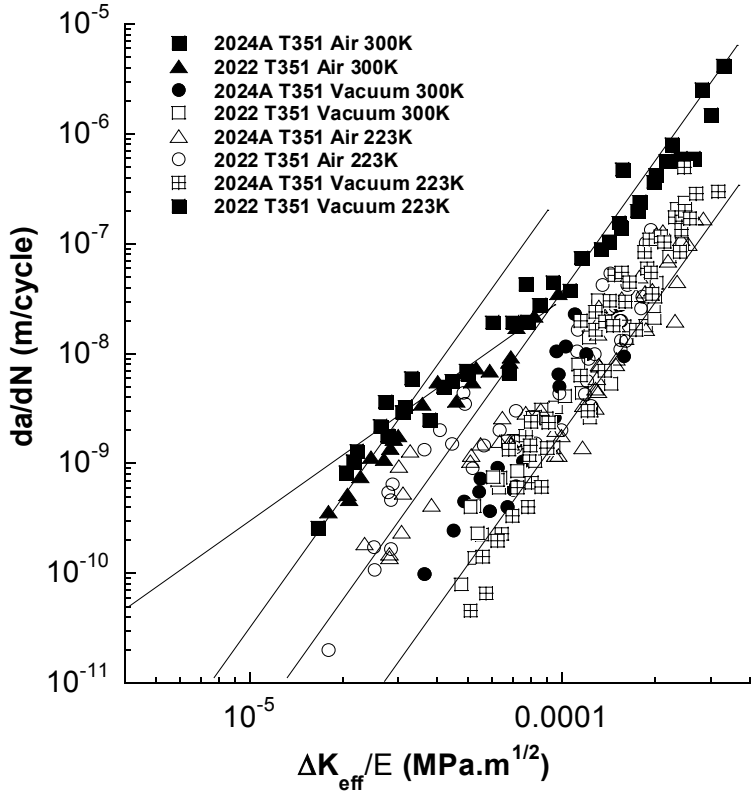

Figure 10: Comparison of the crack propagation rates in air and high vacuum for the naturally aged alloys at 300K and 223K.

Consequently, the higher resistance against crack propagation of the naturally aged temper in cold air as in vacuum has to be related to the underaged microstructure which promotes a crystallographic crack path resulting from slip localization within one slip system within each individual grain along the crack front, such localization being favored by the presence of fine shareable GP zones, as well in dry air as in vacuum.

Finally, such crystallographic crack propagation mechanism prevailing in cold dry air and in high vacuum is in accordance with the intrinsic stage-I like regime with a typical fracture surface morphology as is illustrated in Figure 9b.

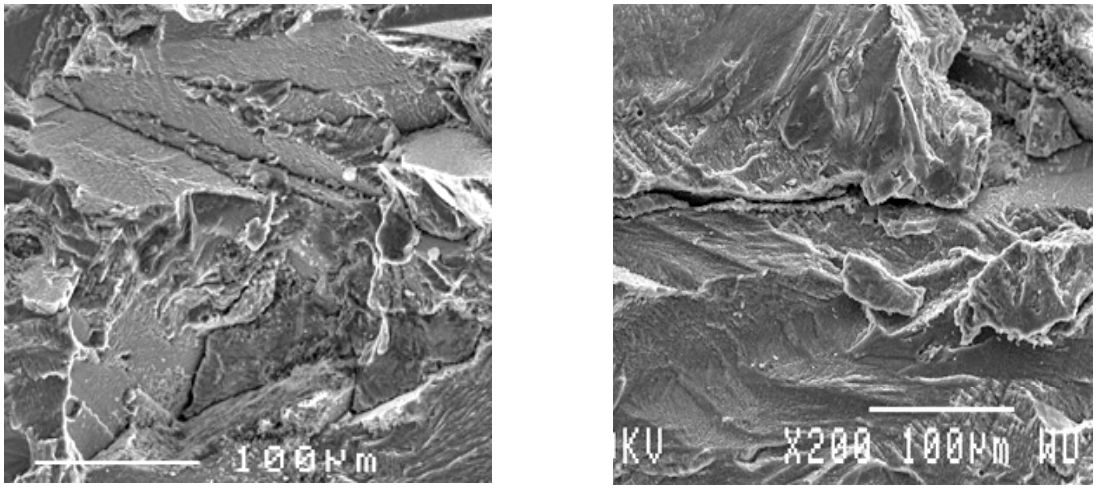

a) b)

Figure 11: fracture surface in cold air: a) da/dN= 10^{-8} m/cycle; b) da/dN= 10^{-10} m/cycle.

However, it is noticeable that in the near threshold domain (da/dN< 10-9 m/cycle), the crystallographic regime prevailing at 223K whatever the environment for the naturally aged alloys at higher growth rates (Figure 11a), switches to a much more flatter crack path (Figure 11b) and faster crack growth rates which becomes in accordance with the intrinsic stage II regime (Figure 10). Such a change may be related to an effect of the remaining 40 ppm of water vapor which could block slip reversibility by a few adsorbed water vapor molecules.

Ongoing detailed experiments, observations and quantification of the surface morphology would give more precise information on the condition governing this cold crack growth regime.

CONCLUSIONS

From this study of the fatigue crack propagation behavior of 2024A T351, 2022 T351 and 2022 T851 alloys at room temperature and 223K, the main following points can be underlined:

- The three alloys present the same fatigue crack propagation behavior in air at room temperature which is characterized by a stage II regime poorly sensitive to microstructure and only affected by the atmospheric humidity in the near-threshold domain;
- At 223K in dry air (dew point of 223K), the crack propagation behavior of the peak aged 2022 T851 is similar to that in ambient air; but the two naturally aged T351 alloys present a highly retarded fatigue crack propagation identified as a crystallographic stage I like regime similar to that observed in high vacuum as well at room temperature as at 223K.

- The naturally aged microstructure (T3 temper) favors such crystallographic stage-I like propagation through the enhancement of planar slip with a localization of the deformation inducing retarded fatigue crack propagation due to a strong barrier at the grain boundaries. The low temperature and the low partial pressure of water vapor both contribute to the initiation of this mechanism.

- A detrimental influence of the dry cold air has been found to take place in the near-threshold domain; it has been related to the presence of the remaining 40 ppm of water vapor, and might be related to an assistance of water vapor adsorption.

REFERENCES

[1] Meyn D A, Transactions of the ASM, 1968; 61(1), 52-61.
[2] Bradshaw J and Wheeler C, Int. J. Fract. Mech 1969; 5(4):255.
[3] Petit J, Fatigue Crack growth Thresholds Concepts, Davidson, D., Suresh eds., TMS-AIME, 1983; 3.
[4] Carter R D, Lee E W, Starke A and Beevers C J., Metallurgical Transactions, 1984; (15A), 555.
[5] Starke, E A and Williams J C, Fracture Mechanics Perspectives and Directions, R P Wei and R.P Gangloff, Eds., ASTM pub., 1989; 184.
[6] Petit J, Hénaff G and Sarrazin-Baudoux C, Comprehensive structural integrity, Volume 6: Fracture of materials from nano to macro; Elsevier Pergamon, 2003; 211.
[7] Gasquères C, Sarrazin-Baudoux C, Petit J and Dumont D, Scripta Mater.; 2005; 53(12), 1333.
[8]. Park K J and Lee S C, Scripta Materialia 1996; 34 (2), 215.
[9] Kirby R B and Beevers C J, Fat. Eng. and Struct., 1979, (1), 203
[10] Petit J and Ranganathan N, Aluminium-Lithium, M. Peters and P.J. Winkler eds., DGM, 1992; (1), 521.
[11] Elber W, Engineering Fracture Mechanics 1970; 2(1), 37.
[12] Petit J, Theoretical and numerical analysis of fatigue, A. Blom and J. Beevers eds., EMAS, 1992; 131.
[13] Petit J, Hénaff G and Sarrazin-Baudoux C, ASTM STP 1372, Newman Jr. J. C. and Piascik R. S. Eds. ASTM pub., 2000; 3.
[14] Suresh S, Vasudevan A K and Bretz P E, Metall. Transactions 1984; (15A), 369.
[15] de los Rios E R, Mohamed H J and Miller K J, Fat. Fract. Engng. Mat. Struct., 1985; 8(1), 49.
[16] Lynch S P, Fatigue Mechanisms, ASTM STP 675, ASTM pub., 1978; 174.
[17] Bouchet B, de Fouquet J, Aguillon M, Acta Metallurgica, 1976; (23), 1325.
[18] Wei R P, ASTM STP 675, ASTM pub., 1979; 816.